(Received 10 May 2024, Accepted 19 June 2024, Scheduled 23 June 2024)

Wave Manipulation with mmWave Wide Bandwidth and Extensive Spatial Coverage Using 1-Bit Reconfigurable Intelligent Surface

Saiful Islam[1], Van Linh Pham[1], Tae Hwan Jang[2], and Hyoungsuk Yoo[1, 3, *]

[1] *Department of Electronic Engineering, Hanyang University, South Korea*
[2] *Department of Electrical Engineering, Hanyang University ERICA, South Korea*
[3] *Department of Biomedical Engineering, Hanyang University, South Korea*

ABSTRACT: We present an advanced approach to wave manipulation utilizing mmWave wide bandwidth, enhanced gain, and extensive spatial coverage through a 1-bit stacked patch reconfigurable intelligent surface (RIS). The RIS was designed on a four-layer board based on RO4350B, featuring a stacked patch on the front and phase-shifter components with a biasing line on the back of board. This sophisticated RIS comprises 400 elements, with a total array size of $100 \times 100\,\text{mm}^2$, providing a remarkable bandwidth of 7.02 GHz to cover the n257 band. Through a meticulous blend of simulations and real-world implementation, we emphasize the adaptability of the RIS in steering beams, maintaining a minimum gain variation and ensuring the gain of 21.03 to 15.17 dBi up to $\pm 80^\circ$ beam steering on normal incidence. Our study explores various beam manipulation scenarios, including near-to-far-field, far-to-far-field, and far-to-near-field transformations. The successful fabrication of the proposed RIS, combined with communication and transmission coefficient performance tests across the n257 band, underscores the practical applicability and robust performance of the system in real-world scenarios, thereby ensuring link throughput. The comprehensive investigation provides valuable insights into the design, simulation, fabrication, and performance evaluation of mmWave RIS. The successful integration of theoretical insights with empirical validations positions the present study at the forefront of mmWave innovation, with significant implications for the future of various research and wireless communication technologies.

1. INTRODUCTION

Reconfigurable Intelligent Surface (RIS) is an innovative technology that uses metasurfaces to dynamically control electromagnetic waves. It can manipulate waves in the millimeter-wave (mmWave) and terahertz range spectrum, offering wide bandwidth and extensive spatial coverage. This technology has significant potential to improve wireless communication and signal propagation, making it highly valuable in research areas such as electromagnetics and optics [1–5]. The fundamental concept behind the RIS involves deploying a surface composed of numerous reconfigurable elements that can alter the properties of the incident electromagnetic waves [6–11]. The RIS can effectively steer and focus signals by intelligently adjusting the phase, amplitude, and polarization of the waves, leading to improved communication links and signal coverage. A conceptual illustration of beam scanning with reconfigurable surfaces for dynamic wave manipulation is shown in Fig. 1.

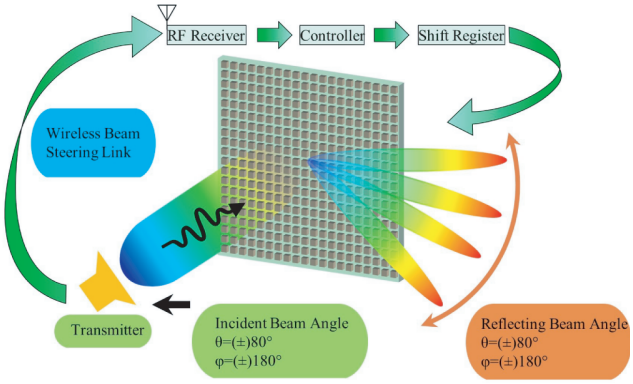

FIGURE 1. Conceptual illustration: Advancements in feedback-based beam scanning with reconfigurable surfaces for dynamic wave manipulation.

Several studies have been conducted on RIS for communication applications. Sub-6 GHz amplifying metasurfaces are presented in [12, 13], where additional radio frequency (RF) amplifiers were introduced to increase the gain. In [14], a computer vision-aided RIS was demonstrated at sub-6 GHz. However, owing to camera-based user detection and the narrow bandwidth of the unit cell, practical applications are limited. Reconfigurable reflectarrays in the X band are presented in [15, 16]. In [15], a three-pin diode-based 1-bit unit cell was developed; however, the realized bandwidth remained narrow. Similarly, in [16], the phase shift remains unstable at the desired operating frequency. Mechanical rotation-based reflectarrays are presented in [17, 18], where a phase difference of 180° was achieved in [17] by altering the position of the unit cell, which

* Corresponding author: Hyoungsuk Yoo (hsyoo@hanyang.ac.kr).

is impractical for most real-world communication applications. Magnetic force-based phase-shifting reflectarrays were demonstrated in [18]; however, the operation bandwidth and beam-scanning range remained narrow. A circularly polarized RIS was demonstrated for the X-band with a two-diode-based 1-bit RIS with a circular patch in [19]. Another one-diode-based 3-bit RIS was presented in [20] that utilized a varactor diode for variable phase shifts. However, for mmWave applications, varactor diode-based RIS development remains challenging owing to the high junction capacitance of varactor diodes. A 1-bit two-split-patch structure-based RIS element was developed in [21]. However, this type of structure produces a narrow bandwidth, which is insufficient for the mmWave 5G frequency bandwidth requirements. Reconfigurable transmitarrays were recognized by utilizing hexagonal resonant patches and pin diodes [22], where two pin diodes are used for 1-bit reconfigurability, enabling two-dimensional (2D) beam scanning. In [23, 24], a liquid crystal-based RIS was developed. Liquid crystals are voltage-sensitive substrates that change their dielectric properties when a voltage is applied on the surface, enabling alteration of the face on the desired elements. Nevertheless, the observed bandwidth of liquid crystal-based RISs remains too narrow for 5G applications. Therefore, they are unsuitable for real-world 5G applications. In [25, 26], a quad polarization and near-field focusing reflectarray, which operates near 15 GHz frequencies range, is presented. An RIS design measurement demonstration was carried out in [27] for the 5.8 GHz band frequency. The RIS comprises two PIN diodes; however, its bandwidth is too narrow for practical applications. Similarly, in [28], five PIN diode-based two RISs were presented to operate at 2.3 and 28 GHz. However, the design process and RIS performance were not well presented for 28 GHz RIS. An X-band two-bit RIS unit cell measurement was presented in [29]; it achieved a wide bandwidth and utilized four PIN diodes. Two PIN diode-based polarization rotating surfaces and a co-aperture dual-frequency programmable metasurface were demonstrated in [30, 31]. A dual-frequency co-aperture structure was formed using two separate structures, where a power divider was used to feed them. In the power divider, a varactor diode was utilized to change the phase of the antenna feeding, which enables it to steer the beam. Evidently, most of the previous research focused on sub-6 GHz or X-bands due to frequency range of n257 (26.50–29.50 GHz), n258 (24.25–27.50 GHz), n261 (27.50–28.35 GHz) is highly sensitive design and fabrication process. RISs are expected to help in current 5G and 6G communications. Therefore, it is crucial to design an RIS in the higher frequency range.

To address some of the aforementioned challenges, we present a design for mmWave RIS with a wide bandwidth and high beam-scanning angles, along with a prototype and validation of its communication performance. In this design, we utilized a stacked patch structure to enhance the bandwidth, gain, and spatial coverage of the elements [32]. In addition, owing to the unstable phase of the stacked patch elements, we incorporated phase-controlled reflective diodes into the microstrip to enhance and maintain the wide bandwidth of the RIS elements, achieving a high reflection of -2.24 dB. We arranged the unit cells in a uniform 20×20 array and performed simulations. Finally, the control circuit and array were fabricated, and their performances were verified in a real-world scenario. The rest of the article is organized into different sections: unit cell design, RIS formulation, RIS fabrication, measured results, and finally, the conclusion.

2. UNIT CELL: DESIGN, SIMULATION, AND DISCUSSION

The unit cell integrates a stacked patch and a 1-bit reflection-type phase shifter. It is designed on a four-layer board, as illustrated in Fig. 2. The substrate material is RO4350B ($\epsilon_r = 3.66$, $\tan\delta = 0.004$), and the prepreg material is RO4450F ($\epsilon_r = 3.52$, $\tan\delta = 0.004$). In the four layers, layer 1 contains a parasitic patch, and layer 2 contains the main patch. Layer 3 is used as the common ground for the antenna and phase shifter and includes DC biasing. Layer 4 comprises a 28 GHz matched impedance microstrip line with lumped components, diodes, and capacitors. The optimized electrical lengths of the microstrip lines are as follows: $E1 = 21.41°$, $E2 = 53.02°$ and 68.91°, based on a 28 GHz wavelength, as illustrated in Fig. 3(a). The phase response of the phase shifter before it is combined with the antenna element is shown in Fig. 3(b). The reflection loss of the phase shifter remains at -2 dB, and the phase response remains consistent within the frequency range of 24–32 GHz, in both ON and OFF cases of the diode. A nearly constant phase difference was observed in Fig. 3(b). In the design process, a flip-chip aluminum gallium arsenide (AlGaAs)

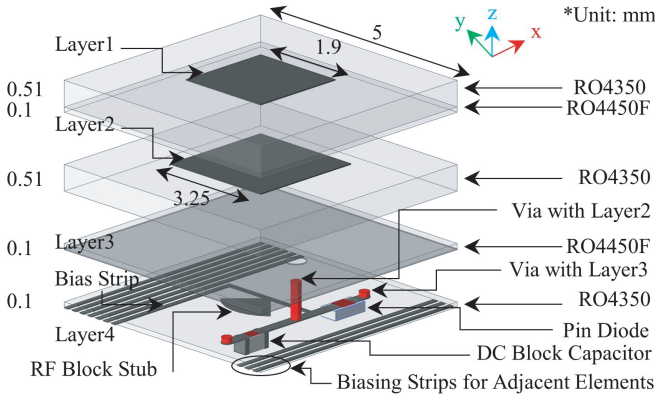

FIGURE 2. Illustration of the unit cell structure: In-depth view along the dimensions.

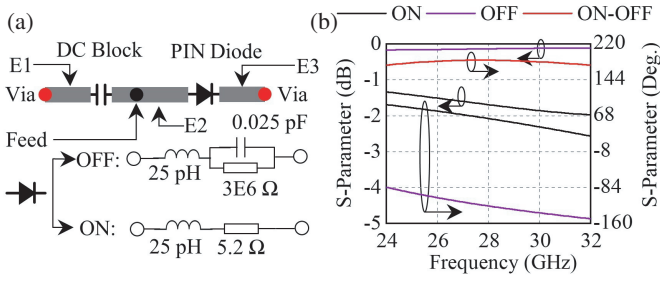

FIGURE 3. Guided wave phase shifter: (a) Microstrip line with lumped elements and (b) scattering parameter response against frequency.

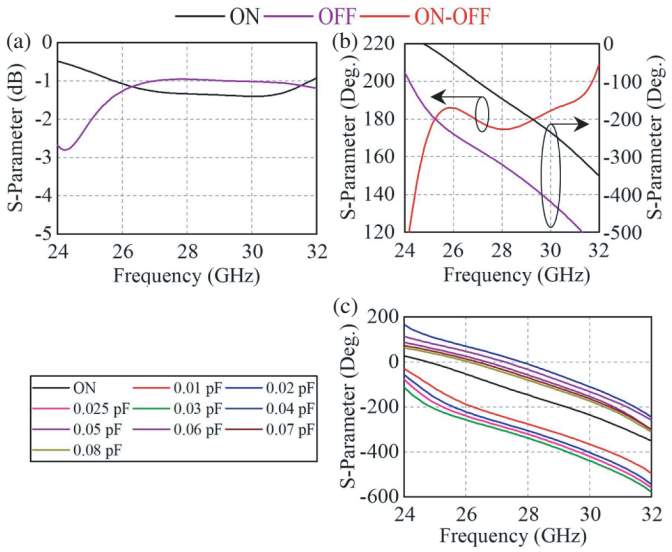

FIGURE 4. Unit cell scattering parameters against frequency: (a) Reflection Loss, (b) phase Response, and (c) parametric Phase Response with the variation of diode capacitance while keeping all other parameters fixed.

PIN diode from MACOM MADP-000907-14020P was used, which operates up to 70 GHz [33] and provides an ultralow capacitance of 0.025 pF under forward-biasing conditions. Additionally, a 100 pF capacitor was used for DC blocking, and an RF choke was employed for RF blocking with the biasing line. Fig. 4 shows the scattering parameters of the unit cell after combining the stacked patch and the phase shifter. It is worth mentioning that the length of the patch elements, feed gap, and small-length adjustments of the matched impedance microstrip line are optimized through rigorous simulations with antenna elements, considering the nonlinear phase response of the antenna. Figs. 4(a) and (b) show the reflection loss and phase response against frequency, respectively. In the normal incident plane, with a phase variation of $\pm 20°$, a wide bandwidth of 7.02 GHz (24.71–31.73 GHz) is maintained, as shown in Fig. 4(b). Within the bandwidth, the maximum reflection loss is -2.4 dB, whereas within the n257 FR2 5G band, the reflection loss remains below -1.4 dB, demonstrating the wide bandwidth and high performance of the unit cell. Additionally, we conducted a parametric analysis of the diode capacitance, as shown in Fig. 4(c). Notably, the diode capacitance plays a vital role in the reflection phase variation of the unit cell. Therefore, it is crucial to consider all the parasitic elements near the unit cell in the simulation environment.

Figure 5 depicts the surface current for both ON and OFF conditions of the diode. In Fig. 5(a), a high current density is observed toward the end of the microstrip line under the ON diode condition when the diode acts as a closed path. However, in Fig. 5(b), under the OFF diode condition, a quarter-phase difference compared to the ON condition can be noticed, with very low current density on the microstrip lines. Similarly, Fig. 5(c) illustrates an exceedingly low current density on the microstrip lines in comparison with the $0°$ ON condition, while Fig. 5(d) also shows low current flowing toward the end. In

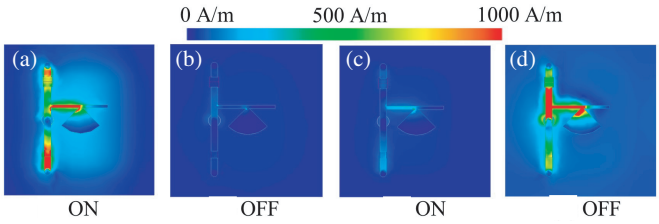

FIGURE 5. Unit cell surface current: (a) and (b) represent the surface current at $0°$ of the induced wave, while (c) and (d) represent the surface current at $90°$ of the induced wave.

the OFF diode conditions, most of the current density is concentrated in the middle section of the microstrip line owing to the diode open condition, and the wave was reflected back to the antenna elements from approximately half of the path of the microstrip line. This microstrip line current path difference produces phase differences in a specified application. These observations highlight the significant effect of the ON and OFF states of the diode on the current distribution along the microstrip line. All EM simulations in the design process were performed using the finite-element-method-based ANSYS HFSS.

3. RIS FORMULATION: DESIGN, SIMULATION, AND DISCUSSION

A stacked patch 1-bit reconfigurable metasurface system in a two-dimensional setup featuring mn radiating elements arranged across the x-y plane and interacting with a feed wave in the (θ_i, ϕ_i) direction is considered. To redirect the primary focus beam precisely to the desired orientation (θ_d, ϕ_d), the excitation phase imposed on the currents of the mn-th element is crucial. Here, (θ_i, ϕ_i) and (θ_d, ϕ_d) can be calculated using x, y, and z of the feed/focus coordinates [17, 34, 35], or vice versa.

$$r_{mn}^{\text{feed}} = \sqrt{(x_{\text{feed}} - x_m)^2 + (y_{\text{feed}} - y_n)^2 + z_{\text{feed}}^2} \quad (1)$$

$$r_{mn}^{\text{focus}} = \sqrt{(x_{\text{focus}} - x_m)^2 + (y_{\text{focus}} - y_n)^2 + z_{\text{focus}}^2} \quad (2)$$

where (x_m, y_n) are the relative coordinates of the (mn)-th element of the array. r_{mn}^{feed} and r_{mn}^{focus} are the distances to the (mn)-th element of the metasurface for each unit cell.

$$\phi_{mn} = k \cdot (r_{mn}^{\text{feed}} + r_{mn}^{\text{focus}}), \quad (3)$$

where ϕ_{mn} denotes the phase distance between the feed, unit cells, and focus point, calculated using Equations (1) and (2).

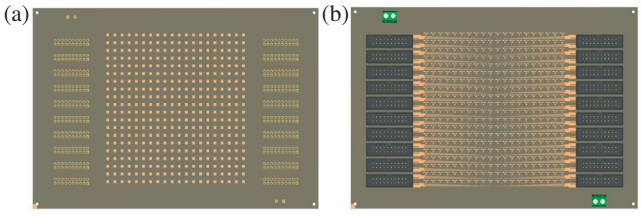

FIGURE 6. Complete RIS along biasing lines and pin headers: (a) Front View, (b) back View.

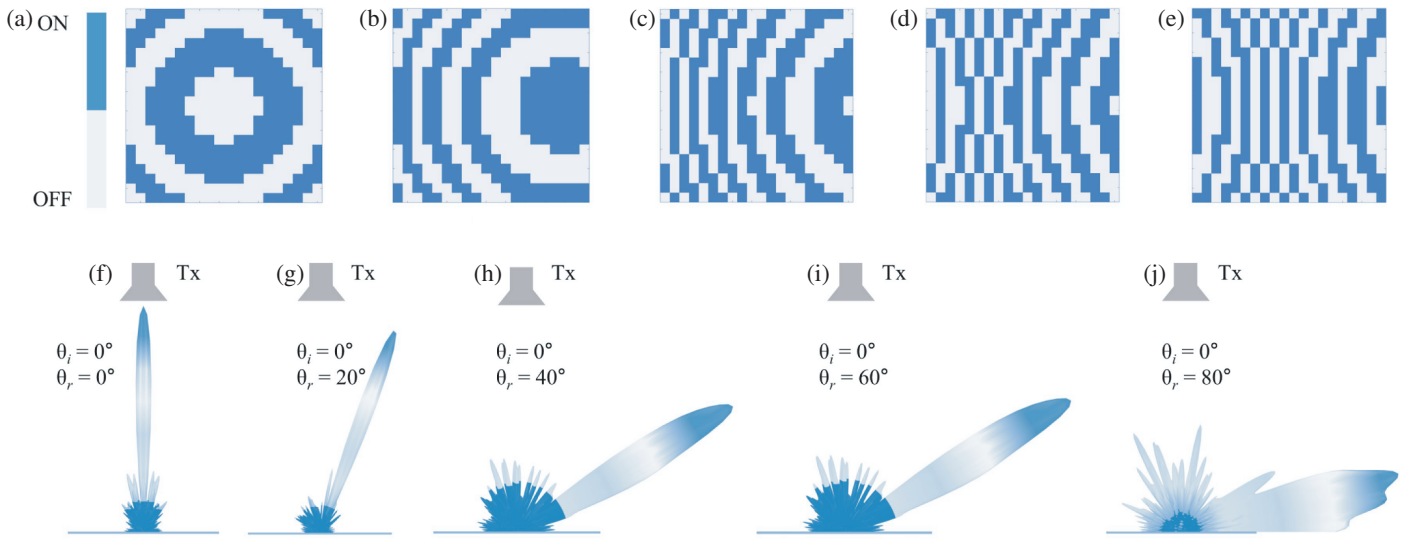

FIGURE 7. Near-field to far-field region beam scanning at different angles with normal incidence: (a) to (e) show the phase pattern of the RIS, and (f) to (j) depict the radiation pattern for 0°, 20°, 40°, 60°, and 80°, respectively.

k denotes the free-space wavenumber. Furthermore, it is modulated at 2π.

For a 1-bit unit cell, the phase must be quantized to manipulate the beam. In our case, we consider state 1 from $-\frac{\pi}{2}$ to $\frac{\pi}{2}$; otherwise, we consider state 0. Therefore, the continuous phase can be quantized as follows:

$$\phi_{mn} = \begin{cases} \pi, & \text{if } -\dfrac{\pi}{2} \leq \phi_{mn} \leq \dfrac{\pi}{2}, \\ 0, & \text{otherwise.} \end{cases} \tag{4}$$

The mathematical representation of the scattering field generated by an incident x- or y-polarized electromagnetic wave onto an RIS comprising $M \times N$ unit cells can be expressed as follows [38]:

$$E(\theta,\varphi) = \sum_{m=0}^{M-1}\sum_{n=0}^{N-1} A_{mn}e^{j\alpha_{mn}} \cdot |\Gamma_{mn}|e^{j\phi_{mn}} \cdot f_{mn}(\theta,\varphi) \times e^{jk_0(md_x \sin\theta\cos\varphi + nd_y \sin\theta\cos\varphi)}, \tag{5}$$

The relative illumination amplitude and phase for each unit cell are denoted by A_{mn} and α_{mn}, respectively. The reflection amplitude and phase of the unit cell (mn) are represented by $|\Gamma_{mn}|$ and ϕ_{mn}. The scattering pattern of the unit cell is given by $f_{mn}(\theta,\phi)$, where dx and dy indicate the spacing between the unit cells in the x and y directions, respectively.

3.1. Array Formation and EM Field Transformation

Figures 6(a) and (b) show complete array front and back views of the RIS, which includes complete biasing networks with pin headers. Excluding the pin headers, the measured surface size was $100 \times 100\,\text{mm}^2$. Fig. 7 illustrates the near-field to far-field transformation at 28 GHz. In the simulation, a horn antenna was used to feed the RIS with a gain of 10.87 dBi. Figs. 7(a)–(e) show the discretized pattern of the RIS for angles of 0°, 20°, 40°, 60°, and 80°, while the feed horn is positioned 100 mm above the surface in normal incidence. The simulated three-dimensional (3D) pattern with gain properties of 21.03, 21.87, 20.59, 17.99, and 15.17 dBi is shown in Figs. 7(f)–(j). The gain deviation is approximately 3 dB up to 60°, and 6 dB at a scan angle of 80°. Figs. 8(a)–(g) show the near-field to far-field beam scanning at different frequencies, ensuring high scanning abilities and wide bandwidth properties of the proposed RIS. It is evident that the gain remains > 14 dBi even at a scanning angle of 80° for operating frequencies of 26, 27, 28, and 29 GHz, and > 12 dBi for the remaining operating frequencies. However, up to $\pm 60°$ scanning angle, the RIS gain remains mostly stable while maintaining a gain of > 18 dBi.

Figures 9(a)–(c) show a normalized electric field (E-field) for the far-field transformation at the frequencies of 27, 28, and 29 GHz. In the simulation environment, a plane wave was fed to the surface at a normal incident angle, and the reflected beam was observed while controlling the surface phase pattern. Beam artifacts exist in the figures owing to the 1-bit phase quantization. However, all beams were successfully translated in the desired direction (scanning angles of 0°–80°).

To validate the proposed RIS further, Fig. 10 demonstrates far-field to near-field region field focusing, offering potential applications in fields such as imaging, radar systems, and quantum physics [36, 37]. In Fig. 10(a), the simulation scenario is illustrated, while Figs. 10(b)–(f) depict near-field beams directed toward desired locations. Specifically, Fig. 10(b) involves feeding at a 30° angle from the positive x-axis and focusing at 15° toward the $-x$-axis at a depth of 600 mm along the z-axis. Fig. 10(c) showcases normal incidence feeding and focusing at 40° toward the $+x$-axis, located at a depth of 600 mm along the z-axis. In Fig. 10(d), normal incidence feeding is combined with focusing at 30° toward the x-axis, situated at a

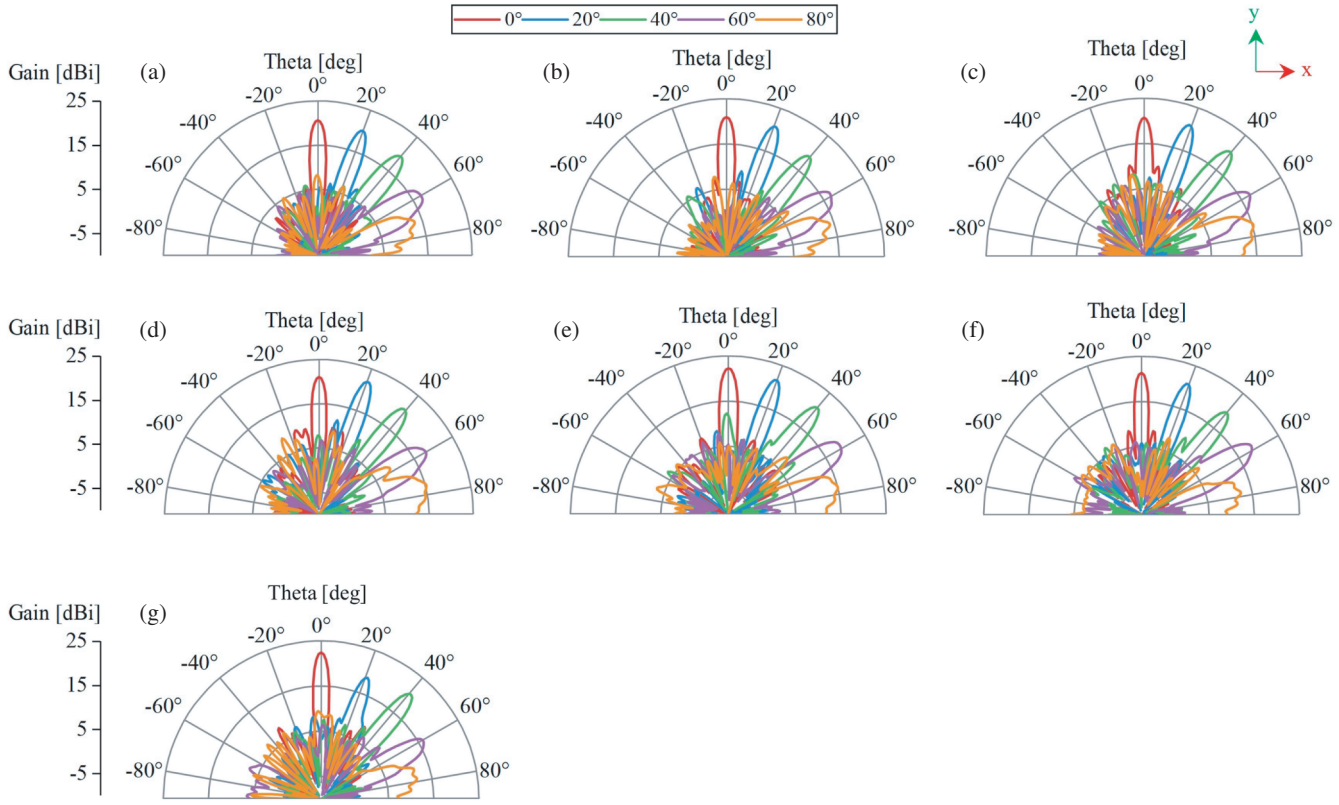

FIGURE 8. Near-field to far-field region beam scanning at different angles with a normal incidence: (a) 25 GHz, (b) 26 GHz, (c) 27 GHz, (d) 28 GHz, (e) 29 GHz, (f) 30 GHz, and (g) 31 GHz.

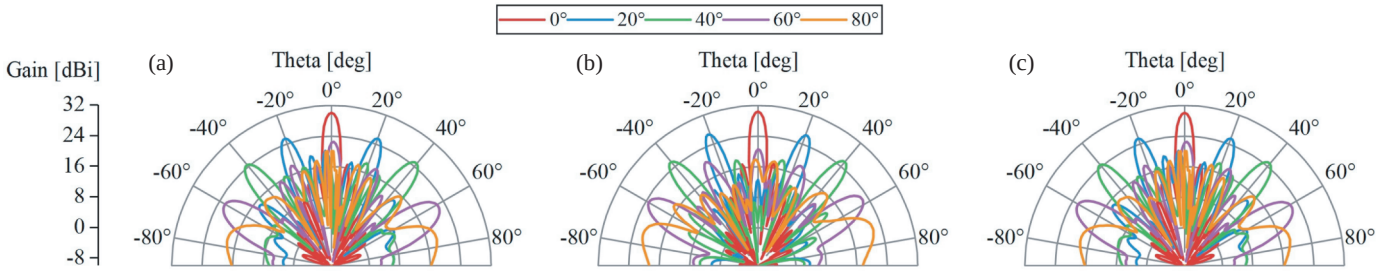

FIGURE 9. Far-field to far-field region beam scanning at different angles with normal incident plane wave: (a) 27 GHz, (b) 28 GHz, and (c) 29 GHz.

depth of 100 mm along the z-axis. Fig. 10(e) demonstrates normal incidence feeding with a focus at the $-x$-axis, set at a 50° angle and directed toward the z-axis at a depth of 300 mm. Finally, Fig. 10(f) exhibits normal incidence feeding with a focus at the $-x$-axis, positioned at a 50° angle and directed toward the z-axis at a depth of 500 mm.

4. RIS MEASUREMENTS RESULTS AND DISCUSSION

To validate the simulation results, we fabricated the RIS and control circuit prototypes shown in Fig. 11 and Fig. 12, respectively. The schematic diagram, illustrating the circuit configuration, is depicted in Fig. 13. The control circuit is required to change the ON/OFF states of the diodes, which consists of 50 shift registers SN74HC595PWR [38], all of which are cascaded to control 400 pin diodes. To maintain consistent current flow to the pin diodes, we utilized an FDN306P MOSFET [39], where the gate of the MOSFET was connected to a shift register output, the source-connected external power source, and the drain was in series with a light-emitting diode (LED), resistor, and pin diode. In the measurement, we use 3 V across the shift register and the common source of the MOSFET and its drains 0.07 A of currents, which indicates low power consumption under the active condition of the RIS.

4.1. Measured Beamforming Communication Performance

The proposed RIS for over-the-air communication was validated to demonstrate its feasibility for real-world applications. The instruments used for the measurement are shown in

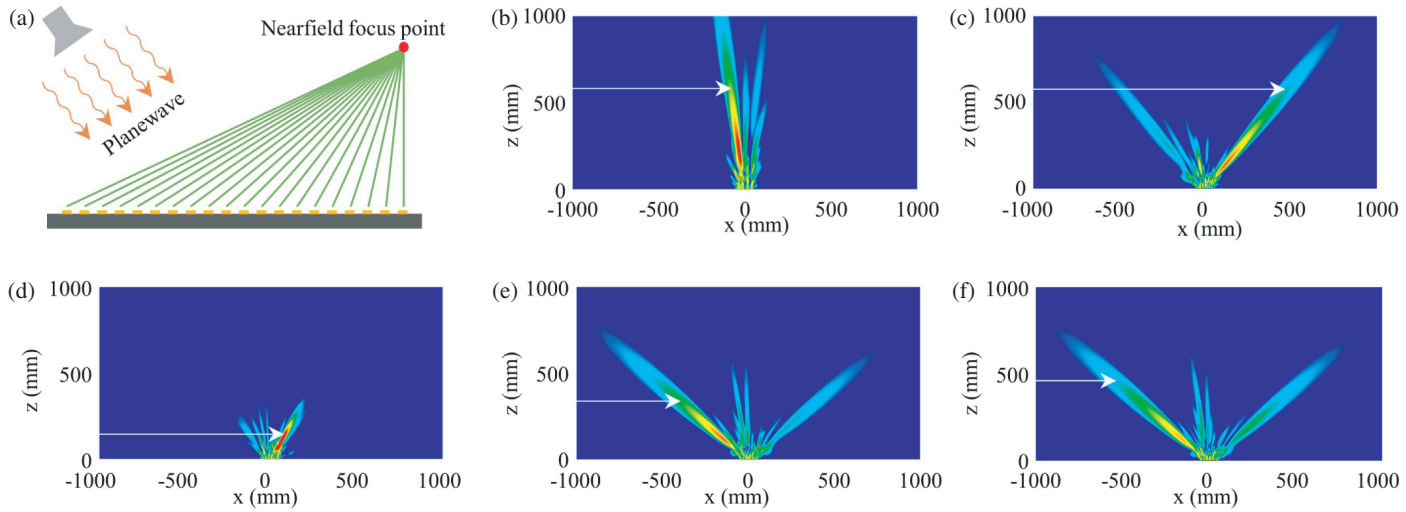

FIGURE 10. Far-field to near-field region field focusing at 28 GHz: (a) Conceptual figure, (b)–(f) field at different depth and angle in the near-field region while having various feeding angles.

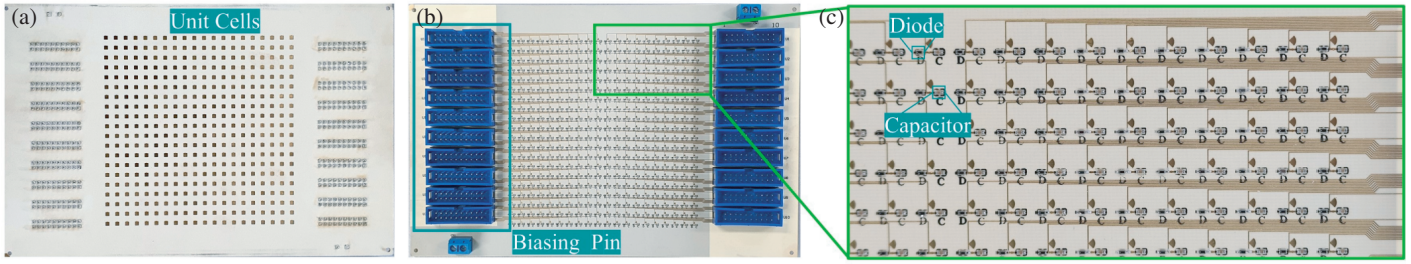

FIGURE 11. Fabricated RIS: (a) Front View, (b) back View, and (c) enlarged View.

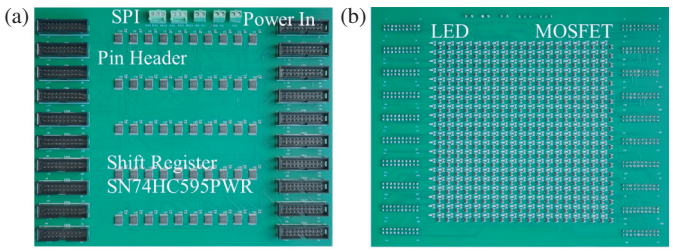

FIGURE 12. Fabricated control circuit: (a) Front view, and (b) back view.

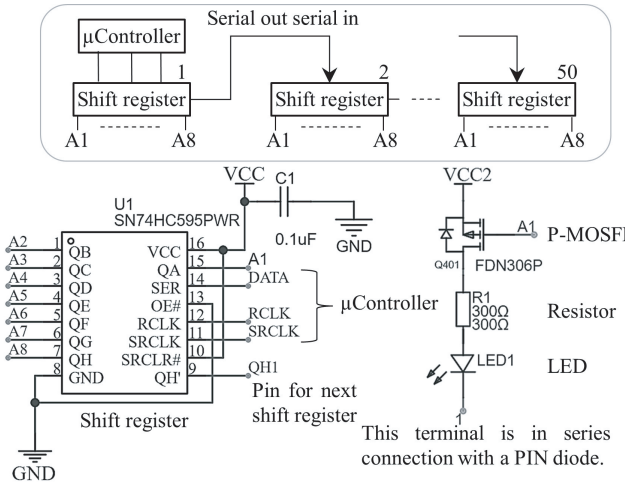

FIGURE 13. Schematic diagram illustrating the connection of a shift register, PMOSFET, resistor, and LED.

Fig. 14. An NI PXIe-3620 IF-LO module was used to first-stage up/down convert the baseband signal and for modulation [40]. Additional up/down converters were used to convert the up/down converted signal from the NI PXIe-3620 to mmWave frequency and vice versa. The mmWave RF front-end beamformer is connected to an mmWave phased array. A 4×4 phased antenna array was employed on the transmitter side, whereas a 4×1 phased antenna array was used on the receiver side.

In the measurement test bed, aimed at analyzing the communication performance of the RIS configuration at different angles and distances at different operating frequencies, an arbitrary wave was generated for the I-Q baseband signal with (64-QAM) at the transmitter side. For both the receiving and transmitting ends, we opted for broadband operation with an 800 MHz bandwidth, satisfying the standard requirements for the 5G NR n257 band. The mmWave frequencies employed were 27, 28, and 29 GHz for each measurement, incorporating

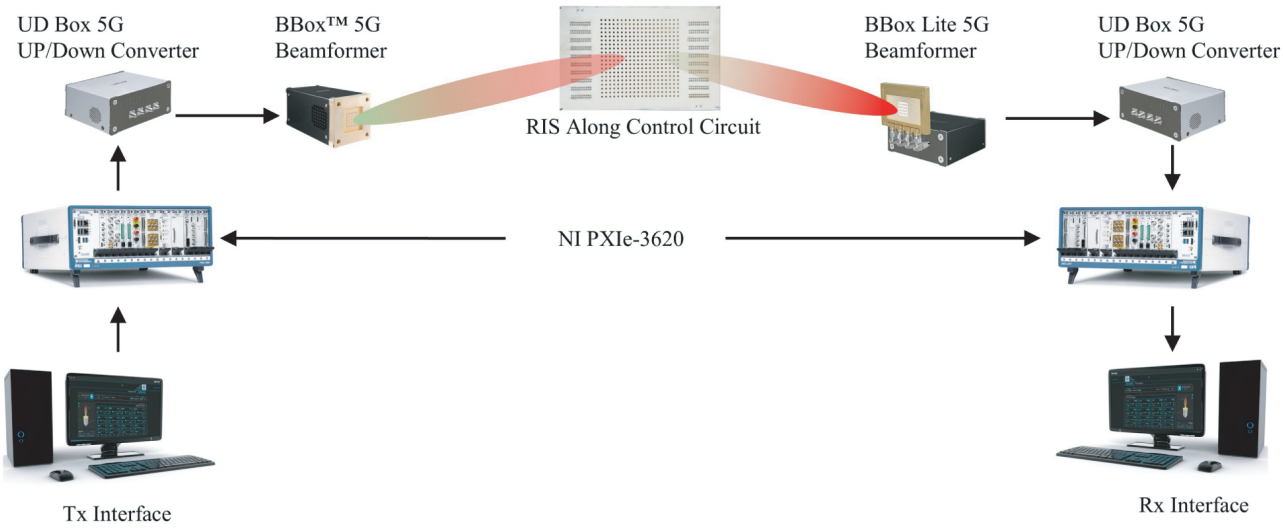

FIGURE 14. Configuration of instruments for mmWave in the testing setup.

TABLE 1. Measurements data composed of constellation diagram, link throughput, Error Vector Magnitude (EVM) for each configuration at the operating frequencies of 27, 28, and 29 GHz.

Frequency		27 GHz			28 GHz			29 GHz		
Distance (m)	Feed	0.8	0.8	0.8	0.5	0.5	0.5	1	1	1
	Focus	1	1	1	0.7	0.7	0.7	2	2	2
Angle	Feed	0°	0°	0°	0°	0°	0°	0°	0°	0°
	Focus	40°	60°	80°	40°	60°	80°	40°	60°	80°
Measured Constellation										
Link Throughput Mbps		1738	1648	1319	1738	1605	1278	1537	1378	1208
EVM (dB)		-25.26	-24.44	-24.20	-25.64	-24.72	-23.67	-25.18	-24.77	-24.14

eight subcarriers, each with a 100 MHz bandwidth. To assess near-field and far-field performance, a test bed featuring transmitter and receiver distances of 1 m, 2 m, 0.5 m, and 0.7 m, is depicted in Figs. 15 and 16, respectively.

Table 1 displays the measured data obtained from the test-bed measurements for the given configuration. The measurement includes a constellation diagram, link throughput, and error vector magnitude (EVM) for each configuration. The results clearly show that the proposed RIS effectively provided satisfactory beam reflection in the desired direction within the operating frequencies of the measurements. At a frequency of 27 GHz, the peak throughput reached 1738 Mbps utilizing a 0.8 m feed and 1 m focus distance at a 40° angle, achieving an EVM of −25.26 dB. At 80° angles, the EVM was −24.20 dB, and the throughput was 1319 Mbps. Moving to 28 GHz, the maximum throughput of 1738 Mbps was recorded with a 0.5 m feed and 0.7 m focus distance, again at 40° angles, with an EVM of −25.64 dB. At 80° angles, the EVM was −23.67 dB, and throughput dropped to 1278 Mbps. Shifting further to 29 GHz, the highest throughput of 1537 Mbps was observed with a 1 m feed and 2 m focus distance at 40° angles, yielding an EVM of −25.18 dB. Similarly, at 80° angles, the EVM was −24.14 dB, and the throughput was 1208 Mbps. Generally, shorter feed distances tended to yield greater throughput, while longer focus distances led to reduced throughput at the same frequency. EVM values exhibited some variability. However, the influence of feed and focus angles on throughput and EVM was less noticeable, which ensures the RIS wide-angle beam scanning capabilities while maintaining acceptable performance. It is worth noting that with the increment of the transmitting antenna power, the throughput and EVM can be improved. However, in our measurement setup, we used the same power for all measurements to understand the RIS behaviors. The constellation diagram provides a visual representation of the signal

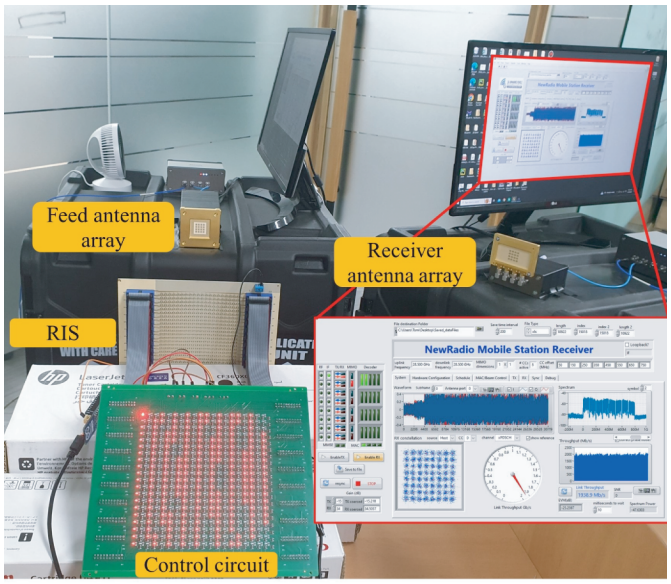

FIGURE 15. Testing the communication performance setup while receiver is at near-field: Positioning the feed antenna array at a distance of 0.5 m from the RIS, and the RIS is located at a distance of 0.7 m from the receiver antenna.

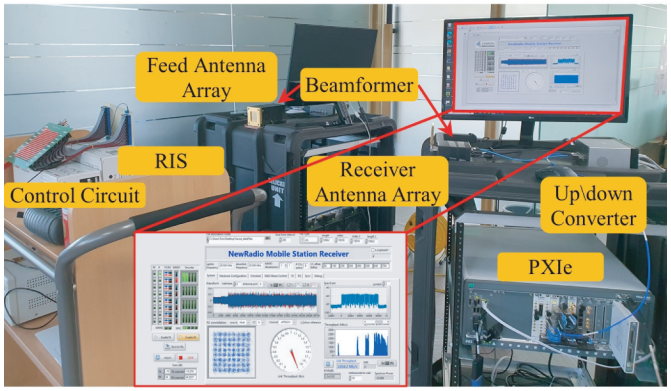

FIGURE 16. Testing the communication performance setup while receiver is at far-field: Positioning the feed antenna array at a distance of 1 m from the RIS, and the RIS is located at a distance of 2 meters from the receiver antenna.

constellations, affirming the integrity and stability of the communication links under various configurations. Link throughput metrics provide insights into the data transfer capabilities of the system, ensuring that the proposed RIS maintains robust performance across different scenarios. The EVM data complemented these findings and offered a quantitative measure of signal quality. The consistently low EVM values observed in the measurements underscore the reliability of the system in maintaining signal fidelity and providing a high transmission coefficient from the RIS. The successful verification of the complete n257 5G NR bandwidth further emphasizes the RIS beam-scanning abilities, ensuring high spatial coverage and highlighting its suitability for advanced wireless communication applications.

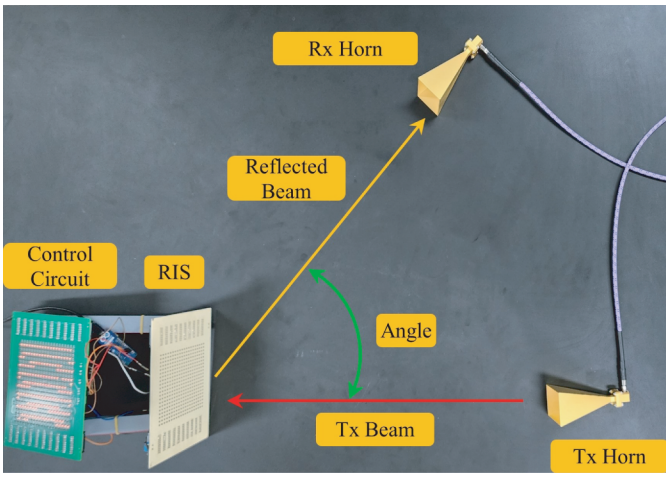

FIGURE 17. Scattering measurement setup with WR-34 Horn antenna.

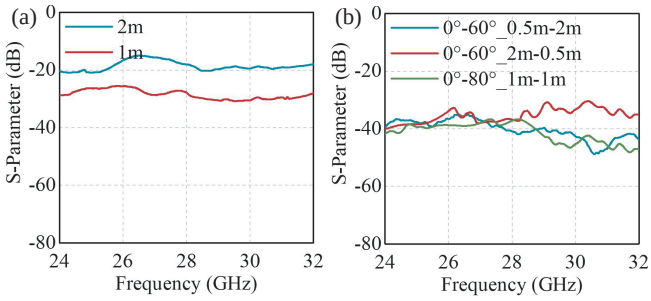

FIGURE 18. Measured scattering parameters: (a) Feed horn and receiver horn when aligned face to face, (b) quantization phase frequency of 28 GHz.

4.2. Measured Transmission Coefficient and Radiation Pattern

We further measured the RIS transmission parameters using two horn antenna setups, where one was used as a transmitter (Tx) and the other as a receiver (Rx), as shown in Fig. 17. For measurements, we used Anritsu MS46122V vector network analyzer along with two WR-34 horn antennas (22 to 33 GHz) with a gain of 20 dBi. Fig. 18(a) shows the Tx horn to Rx horn scattering parameters for two different setups: one with the horns 1 m apart and the other with the horns 2 m apart, both facing each other. The 1 m apart setup shows a transmission coefficient about -20 dB (± 5 dB) over the frequency range of 24 GHz to 32 GHz. Similarly, the 2 m apart setup shows a transmission coefficient about -30 dB (± 5 dB). Fig. 18(b) presents the scattering parameters for three different setups: (a) Beam steering at 60° with normal incidence when the transmitter is 0.5 m from the RIS and the receiver 2 m from the RIS. (b) Normal incidence and 60° beam steering with a 2-m transmitter distance and a 0.5-m receiver distance. (c) Normal incidence and 80° beam steering with both the transmitter and receiver 1 m from the RIS. For all these measurement setups, the transmission coefficient remains about -40 dB (± 5 dB) when the bit quantization frequency is 28 GHz.

Similarly, Fig. 19 shows the scattering parameters for different frequencies from 24 GHz to 32 GHz with 1 GHz steps. In this measurement setup, the Tx and Rx were 0.5 m away from

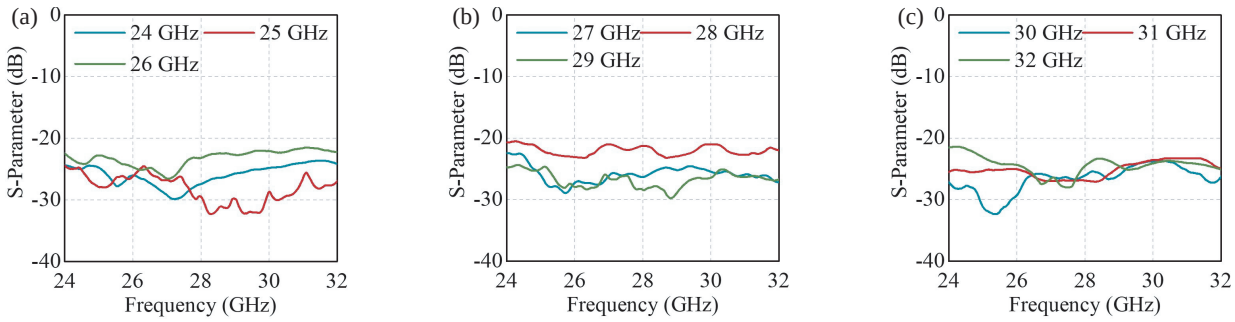

FIGURE 19. Measured scattering parameters with the Tx horn at a 0° angle and the Rx horn antenna at a 60° angle, both located 0.5 m from the RIS, at quantization phase frequencies of (a) 24, 25, and 26 GHz, (b) 27, 28, and 29 GHz, and (c) 30, 31, and 32 GHz.

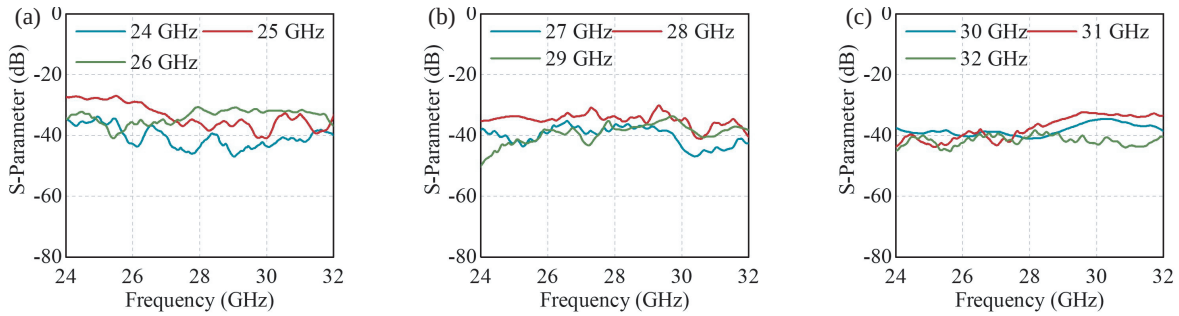

FIGURE 20. Measured scattering parameters with the Tx horn located 1 m from the RIS at a 0° angle and the Rx horn antenna located 1 m from the RIS at a 60° angle, at quantization phase frequencies of (a) 24, 25, and 26 GHz, (b) 27, 28, and 29 GHz, and (c) 30, 31, and 32 GHz.

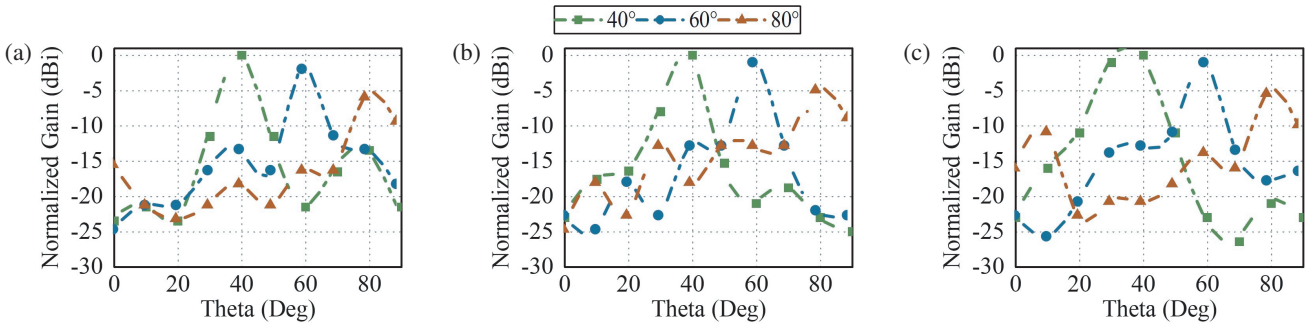

FIGURE 21. Measured radiation pattern of RIS at 40°, 60°, and 80° angle for the frequencies: (a) 27 GHz, (b) 28 GHz, and (c) 29 GHz.

the RIS, with the Tx normal to the surface and the Rx at a 60° angle for all measurements and phase quantization at the respective operating frequency. The results show that the transmission coefficient remains about −25 dB (±7 dB). It is worth noting that, as this is a scattering parameter-based measurement with a wideband transmission coefficient, slight misalignment significantly reduces the transmission coefficient due to the narrow gain properties of the RIS. However, this measurement ensures the wideband operation of the RIS compared to Fig. 18(a), where the total distance 1-m apart with RIS reflections setup shows a 5 dB lower transmission coefficient than the direct horn antenna face-to-face setup, usually due to imperfect alignment of the horn antenna beam with the RIS. Additional small losses of the RIS can be found in Fig. 4(a). Furthermore, Fig. 20 shows the transmission coefficient for a setup similar to Fig. 19 but with the Tx and Rx extended to 1 m from the RIS. In this measurement, the transmission coefficient remains about −38 dB (±8 dB), demonstrating the RIS operability in a wider-angle, wideband, and far-field region. The transmission can be further improved with active beam controlling mechanisms, which can automatically align the beam with the receiver and transmitter.

Additionally, Figs. 21(a)–(c) present the measured normalized radiation patterns at 27, 28, and 29 GHz, respectively, for normal incidence, while incorporating scanning angles of 40°, 60°, and 80°. The measurement results demonstrate effective beam focusing at various angles and frequencies. For pattern measurement, the feed antenna was positioned at a distance of 1 m, and the receiver antenna was located at a distance of 2 m. The results highlight the versatility of the proposed system in

TABLE 2. Comparison with state-of-the-art RIS.

Ref. No.	Method	Number of elements	Frequency (GHz)	Bandwidth (GHz)	Size (mm^2)	Test-bed communication	Scan range
[20]	Single varactor diodes	100	3.2	3.00–3.35	254×272	No	$\theta = (\pm)60^\circ$
[21]	Single diode	400	35	34.20–36.15	100×100	No	$\theta = (\pm)45^\circ$ & $\phi = (\pm)180^\circ$
[24]	Liquid crystal	144	29.5	N/A	60×60	Yes	$\theta = (\pm)62^\circ$
[41]	2 PIN diodes	256	73	70.30–75.3	32×32	No	$\theta = (\pm)70^\circ$
[42]	Single diode	400	27.5	22.70–30.50	77×77	No	$\theta = (\pm)50^\circ$ & $\phi = (\pm)180^\circ$
[Proposed]	**Single diode**	**400**	**28**	**24.71–31.73**	**100×100**	**Yes**	$\theta = (\pm)80^\circ$ & $\phi = (\pm)180^\circ$

achieving targeted beam patterns across different scanning angles and operating frequencies.

4.3. Comparison with State-of-the-Art RIS

We conducted a state-of-the-art comparison with previous publications, presenting various findings in comparison with the proposed RIS, as enlisted in Table 2. The table demonstrates a comparison based on some major requirements and properties of the RIS, recognizing that each individual work has unique intended gains in performance. In [20], a single varactor diode was employed for continuous phase shifting by altering the voltage, suitable for sub-6 GHz applications but facing limitations at mmWave 5G bands. Similarly, [24] utilized a single pin diode at mmWave frequencies, but the achieved bandwidth fell short of 5G requirements. Another technique using liquid crystal-based RIS in [24] demonstrated beam scanning in one axis with very narrow bandwidths, indicating limitations. An E-band RIS in [41] incorporated two pin diodes to enhance performance, and the recent work in [42] tackled the narrow bandwidth issue with a rounded corner-based patch structure, achieving a stable beam scanning angle of 50°.

To address previous limitations comprehensively, we developed a wideband and wide-scanning-angle RIS using a stacked patch, enhancing bandwidth, gain, and spatial coverage. Additionally, we demonstrated field transformation in different regions and frequencies. Furthermore, our work includes the establishment of a testbed measurement setup to ensure that the RIS reflects communication performance across a wide range of frequencies and angles, a feature absent in many previous works [20, 21, 41, 42]. While we have addressed several limitations present in previous publications, we recognize that our proposed work still has potential for further improvement. Increasing the number of bits could help suppress mirror patterns more effectively. Additionally, incorporating dual polarization capabilities would significantly enhance the overall performance and versatility of our design while maintaining wide bandwidth and beam-scanning abilities. We hope to achieve these improvements and attain the desired performance in our future work.

5. CONCLUSION

We introduced a mmWave wideband RIS with high spatial coverage across the entire operating range. The designed RIS comprises 400 elements, with each element measuring $5 \times 5\,mm^2$, effectively operating in the frequency range of 24.71–31.73 GHz. In our simulation environments, we demonstrated the effectiveness of the RIS throughout its operation bandwidth. With a gain variation of approximately 6 dBi, the beam pattern can be steered up to 80°, significantly enhancing the spatial coverage for operation. Furthermore, we demonstrated the capability of the RIS for beam manipulation in various scenarios, including near-to-far-field, far-to-far-field, and far-to-near-field transformations. The simulation results illustrated the adaptability and versatility of the proposed RIS for steering beams under different operational conditions. Moving beyond the simulations, we successfully fabricated the proposed RIS along with a control circuit. Additionally, we conducted communication performance tests under various conditions across the n257 band to demonstrate the practical applicability and robustness of the proposed system in real-world scenarios. The results provided a comprehensive understanding of the capabilities of the RIS, from its design and simulation to its fabrication and performance evaluation.

ACKNOWLEDGEMENT

This work was supported by the Institute of Information and Communications Technology Planning and Evaluation (IITP) Grant funded by the Korean Government Ministry of Science and ICT (MIST) under Grant 2022-0-00310).

APPENDIX A.

To automate the beam tracking from the RIS, we propose the procedure outlined in Algorithm 1. The algorithm uses 915 MHz RF links for communication between base stations and the RIS. The RIS actively searches for the optimum beam based on feedback received from the base station, which is derived from the link performance between the base station and receiver devices. Although we evaluated wireless bit transmis-

sion through the 915 MHz RF link, an automatic beam-tracking test could not be conducted in real time owing to limitations in the measurement system. Nevertheless, this study provides valuable insights into future possibilities.

Algorithm 1 Beam Tracking with SNR Threshold

Input: Initialize base station beam angle towards the RIS.
Input: Initialize RIS beam angle towards the mobile user.
Loop:
TransmitCommandToRISController()
{Transmit a command to the RIS to initiate scanning through the 915 MHz RF link.}
Wait for acknowledgment or timeout.
if AcknowledgmentReceived() **then**
  MeasureSNRatBaseStation()
  {Measure SNR for the beam from the RIS towards the mobile user.}
  if SNR > SNRThreshold **then**
    KeepRISBeamAtCurrentAngle()
  else
    AdjustRISBeamAngle()
  end if
else
  HandleTimeout()
  {Handle the timeout situation (e.g., retry or take appropriate action).}
end if
Repeat the loop as needed.

REFERENCES

[1] Basar, E., M. D. Renzo, J. D. Rosny, M. Debbah, M.-S. Alouini, and R. Zhang, "Wireless communications through reconfigurable intelligent surfaces," *IEEE Access*, Vol. 7, 116 753–116 773, 2019.

[2] ElMossallamy, M. A., H. Zhang, L. Song, K. G. Seddik, Z. Han, and G. Y. Li, "Reconfigurable intelligent surfaces for wireless communications: Principles, challenges, and opportunities," *IEEE Transactions on Cognitive Communications and Networking*, Vol. 6, No. 3, 990–1002, 2020.

[3] Lin, P., C. Qian, J. Zhang, J. Chen, X. Zhu, Z. Wang, J. Huangfu, and H. Chen, "Enabling intelligent metasurfaces for semi-known input," *Progress In Electromagnetics Research*, Vol. 178, 83–91, 2023.

[4] Liu, Y., X. Liu, X. Mu, T. Hou, J. Xu, M. D. Renzo, and N. Al-Dhahir, "Reconfigurable intelligent surfaces: Principles and opportunities," *IEEE Communications Surveys & Tutorials*, Vol. 23, No. 3, 1546–1577, 2021.

[5] Tang, W., M. Z. Chen, X. Chen, J. Y. Dai, Y. Han, M. D. Renzo, Y. Zeng, S. Jin, Q. Cheng, and T. J. Cui, "Wireless communications with reconfigurable intelligent surface: Path loss modeling and experimental measurement," *IEEE Transactions on Wireless Communications*, Vol. 20, No. 1, 421–439, 2021.

[6] Zhou, E., Y. Cheng, F. Chen, H. Luo, and X. Li, "Low-profile high-gain wideband multi-resonance microstrip-fed slot antenna with anisotropic metasurface," *Progress In Electromagnetics Research*, Vol. 175, 91–104, 2022.

[7] Yuan, X., Y.-J. A. Zhang, Y. Shi, W. Yan, and H. Liu, "Reconfigurable-intelligent-surface empowered wireless communications: Challenges and opportunities," *IEEE Wireless Communications*, Vol. 28, No. 2, 136–143, 2021.

[8] Ji, W., J. Chang, H.-X. Xu, J. R. Gao, S. Gröblacher, H. P. Urbach, and A. J. L. Adam, "Recent advances in metasurface design and quantum optics applications with machine learning, physics-informed neural networks, and topology optimization methods," *Light: Science & Applications*, Vol. 12, No. 1, 169, 2023.

[9] El Badawe, M. and O. M. Ramahi, "Efficient metasurface rectenna for electromagnetic wireless power transfer and energy harvesting," *Progress In Electromagnetics Research*, Vol. 161, 35–40, 2018.

[10] Ahmed, F., T. Hassan, N. Melouki, H. Naseri, P. PourMohammadi, A. Iqbal, and T. A. Denidni, "A multi-bit and frequency-reconfigurable reflecting surface for RIS applications," *IEEE Antennas and Wireless Propagation Letters*, Vol. 23, No. 2, 653–657, 2023.

[11] Li, H.-P., G.-M. Wang, J.-G. Liang, and X.-J. Gao, "Wideband multifunctional metasurface for polarization conversion and gain enhancement," *Progress In Electromagnetics Research*, Vol. 155, 115–125, 2016.

[12] Wu, L., K. Lou, J. Ke, J. Liang, Z. Luo, J. Y. Dai, Q. Cheng, and T. J. Cui, "A wideband amplifying reconfigurable intelligent surface," *IEEE Transactions on Antennas and Propagation*, Vol. 70, No. 11, 10 623–10 631, 2022.

[13] Xia, D., X. Wang, J. Han, H. Xue, G. Liu, Y. Shi, L. Li, and T. J. Cui, "Accurate 2-D DoA estimation based on active metasurface with nonuniformly periodic time modulation," *IEEE Transactions on Microwave Theory and Techniques*, Vol. 71, No. 8, 3424–3435, 2023.

[14] Ouyang, M., F. Gao, Y. Wang, S. Zhang, P. Li, and J. Ren, "Computer vision-aided reconfigurable intelligent surface-based beam tracking: Prototyping and experimental results," *IEEE Transactions on Wireless Communications*, Vol. 22, No. 12, 8681–8693, 2023.

[15] Cao, X., Q. Chen, T. Tanaka, M. Kozai, and H. Minami, "A 1-bit time-modulated reflectarray for reconfigurable-intelligent-surface applications," *IEEE Transactions on Antennas and Propagation*, Vol. 71, No. 3, 2396–2408, 2023.

[16] Ning, Y., S. Zhu, H. Chu, Q. Zou, C. Zhang, J. Li, P. Xiao, and G. Li, "1-bit low-cost electronically reconfigurable reflectarray and phased array based on p-i-n diodes for dynamic beam scanning," *IEEE Transactions on Antennas and Propagation*, Vol. 72, No. 2, 2007–2012, 2023.

[17] Mei, P., S. Zhang, and G. F. Pedersen, "A low-cost, high-efficiency and full-metal reflectarray antenna with mechanically 2-D beam-steerable capabilities for 5G applications," *IEEE Transactions on Antennas and Propagation*, Vol. 68, No. 10, 6997–7006, 2020.

[18] Hu, A., K. Konno, Q. Chen, and T. Takahashi, "A highly efficient 1-bit reflectarray antenna using electromagnets-controlled elements," *IEEE Transactions on Antennas and Propagation*, Vol. 72, No. 1, 506–517, 2023.

[19] Wu, F., R. Lu, J. Wang, Z. H. Jiang, W. Hong, and K.-M. Luk, "A circularly polarized 1 bit electronically reconfigurable reflectarray based on electromagnetic element rotation," *IEEE Transactions on Antennas and Propagation*, Vol. 69, No. 9, 5585–5595, 2021.

[20] Liang, J. C., Q. Cheng, Y. Gao, C. Xiao, S. Gao, L. Zhang, S. Jin, and T. J. Cui, "An angle-insensitive 3-bit reconfigurable intelligent surface," *IEEE Transactions on Antennas and Propagation*, Vol. 70, No. 10, 8798–8808, 2022.

[21] Han, J., L. Li, S. Tian, G. Liu, H. Liu, and Y. Shi, "Millimeter-wave imaging using 1-bit programmable metasurface: Simulation model, design, and experiment," *IEEE Journal on Emerging and Selected Topics in Circuits and Systems*, Vol. 10, No. 1, 52–61, 2020.

[22] Xi, B., Y. Xiao, H. Dong, M. Xiang, F. Yang, and Z. Chen, "Low-profile wideband 1-bit reconfigurable transmitarray with 2-D beam-scanning capacity," *IEEE Transactions on Antennas and Propagation*, Vol. 71, No. 4, 3228–3237, 2023.

[23] Kim, H., S. Oh, S. Bang, H. Yang, B. Kim, and J. Oh, "Independently polarization manipulable liquid-crystal-based reflective metasurface for 5G reflectarray and reconfigurable intelligent surface," *IEEE Transactions on Antennas and Propagation*, Vol. 71, No. 8, 6606–6616, 2023.

[24] Youn, Y., D. An, D. Kim, M. Hwang, H. Choi, B. Kang, and W. Hong, "Liquid crystal-driven reconfigurable intelligent surface with cognitive sensors for self-sustainable operation," *IEEE Transactions on Antennas and Propagation*, Vol. 71, No. 12, 9415–9423, 2023.

[25] Wu, X., Z. Li, Z. Zhang, X. Wang, L. Si, and W. Zhu, "Mechanically reconfigurable folded reflectarray antenna for variable near-field focusing," *IEEE Transactions on Antennas and Propagation*, Vol. 71, No. 12, 10 038–10 043, 2023.

[26] Yu, H., Z. Zhang, J. Su, M. Qu, Z. Li, S. Xu, and F. Yang, "Quad-polarization reconfigurable reflectarray with independent beam scanning and polarization switching capabilities," *IEEE Transactions on Antennas and Propagation*, Vol. 71, No. 9, 7285–7298, 2023.

[27] Pei, X., H. Yin, L. Tan, L. Cao, Z. Li, K. Wang, K. Zhang, and E. Björnson, "RIS-aided wireless communications: Prototyping, adaptive beamforming, and indoor/outdoor field trials," *IEEE Transactions on Communications*, Vol. 69, No. 12, 8627–8640, 2021.

[28] Dai, L., B. Wang, M. Wang, X. Yang, J. Tan, S. Bi, S. Xu, F. Yang, Z. Chen, M. D. Renzo, C.-B. Chae, and L. Hanzo, "Reconfigurable intelligent surface-based wireless communications: Antenna design, prototyping, and experimental results," *IEEE Access*, Vol. 8, 45 913–45 923, 2020.

[29] Ma, X., J. Han, T. Wang, S. Chen, Y. Mu, H. Liu, and L. Li, "Design and rectangular waveguide validation of 2-bit wideband reconfigurable reflective metasurface element in x-band," *IEEE Antennas and Wireless Propagation Letters*, Vol. 22, No. 1, 4–8, 2023.

[30] Hu, W. S., Y. H. Liu, C. Y. Gong, S. Y. Wang, and Y. B. Li, "Dual-frequency co-aperture control of beam scanning by programmable metasurface," *IEEE Antennas and Wireless Propagation Letters*, Vol. 22, No. 12, 3013–3017, 2023.

[31] Luyen, H., Z. Zhang, J. H. Booske, and N. Behdad, "Wideband, beam-steerable reflectarray antennas exploiting electronically reconfigurable polarization-rotating phase shifters," *IEEE Transactions on Antennas and Propagation*, Vol. 70, No. 6, 4414–4425, 2022.

[32] Liu, Z.-F., P.-S. Kooi, L.-W. Li, M.-S. Leong, and T.-S. Yeo, "A method for designing broad-band microstrip antennas in multilayered planar structures," *IEEE Transactions on Antennas and Propagation*, Vol. 47, No. 9, 1416–1420, 1999.

[33] MACOM, "Madp-000907-14020p," Available: https://www.macom.com/products/product-detail/MADP-000907-14020P.

[34] Amri, M. M., N. M. Tran, and K. W. Choi, "Reconfigurable intelligent surface-aided wireless communications: Adaptive beamforming and experimental validations," *IEEE Access*, Vol. 9, 147 442–147 457, 2021.

[35] Ning, Y., S. Zhu, H. Chu, Q. Zou, C. Zhang, J. Li, P. Xiao, and G. Li, "1-bit low-cost electronically reconfigurable reflectarray and phased array based on p-i-n diodes for dynamic beam scanning," *IEEE Transactions on Antennas and Propagation*, Vol. 72, No. 2, 2007–2012, 2023.

[36] Kashyap, B. G., P. C. Theofanopoulos, Y. Cui, and G. C. Trichopoulos, "Mitigating quantization lobes in mmWave low-bit reconfigurable reflective surfaces," *IEEE Open Journal of Antennas and Propagation*, Vol. 1, 604–614, 2020.

[37] Vabichevich, D., A. Belov, and A. Sayanskiy, "Suppression of quantization lobes in 1-bit reconfigurable intelligent surfaces," *IEEE Antennas and Wireless Propagation Letters*, Vol. 22, No. 12, 2808–2811, 2023.

[38] Instruments, T., "SN74HCT595 8-bit shift register with tll-compatible CMOS inputs and 3-state output registers," Available: https://www.ti.com/product/SN74HCT595.

[39] Onsemi, "MOSFETs — FDN306P P-Channel 1.8V Specified PowerTrench® MOSFET -12 V, -2.6 A, 40 mOhm," Available: https://www.onsemi.com/products/discrete-power-modules/mosfets/FDN306P.

[40] Instruments, N., "Pxie-3620 rf upconverter and downconverter module," Available: https://www.ni.com/docs/en-US/bundle/mmwave-transceiver-system-specs/page/specs.html.

[41] Liu, C., F. Yang, S. Xu, and M. Li, "An e-band reconfigurable reflectarray antenna using p-i-n diodes for millimeter-wave communications," *IEEE Transactions on Antennas and Propagation*, Vol. 71, No. 8, 6924–6929, 2023.

[42] Wang, R., Y. Yang, B. Makki, and A. Shamim, "A wideband reconfigurable intelligent surface for 5G millimeter-wave applications," *IEEE Transactions on Antennas and Propagation*, Vol. 72, No. 3, 2399–2410, 2024.